Journal of Materials Chemistry A

RSC Publishing

PAPER

View Article Online
View Journal | View Issue

Cite this: J. Mater. Chem. A, 2013, 1, 919

A new strategy for the surface-free-energy-distribution induced selective growth and controlled formation of Cu_2O–Au hierarchical heterostructures with a series of morphological evolutions†

Han Zhu,[b] MingLiang Du,*[ab] DongLiang Yu,[b] Yin Wang,[c] LiNa Wang,[a] MeiLing Zou,[b] Ming Zhang[ab] and YaQin Fu[ab]

Received 7th October 2012
Accepted 23rd October 2012

DOI: 10.1039/c2ta00591c

www.rsc.org/MaterialsA

A strategy of surface-free-energy-distribution induced selective growth of Au nanograins (AuNGs) on specific positions of Cu_2O octahedron surfaces with a series of morphological evolutions has been demonstrated. The surface energy distribution of Cu_2O octahedra generally follows the order of {111} facets < crystal edges < vertices and leads to the preferential growth and evolution of the heterostructures. The morphological evolutions and crystal structures of Cu_2O and Cu_2O–Au hierarchical heterostructures are investigated and discussed. Meanwhile, Cu_2O octahedra coated by different amounts of polyvinyl pyrrolidone (PVP) and $HAuCl_4$ were taken as control and the results indicate that the trend in the selective growth on PVP coated Cu_2O octahedra decreased significantly because of the reducing diversity of the surface-free-energy-distribution. The identity and crystal phase structures of these Cu_2O, Cu_2O–Au and Cu_2O–PVP–Au heterostructures are manifested through X-ray diffraction (XRD) and energy-dispersive X-ray spectrometers (EDS). X-ray photoelectron spectroscopy (XPS) further probes the surface chemical compositions and chemical oxidation state of the as-prepared Cu_2O and Cu_2O–Au hierarchical heterostructures and test the galvanic reaction between Cu_2O and $AuCl_4^-$. The growth mechanism of the surface-free-energy-distribution induced selective growth of AuNGs on Cu_2O octahedra with morphological evolution is also discussed. The photocatalytic performances of the as-prepared Cu_2O and Cu_2O–Au hierarchical heterostructures for the degradation of methyl orange (MO) are investigated and the results suggest the substantially enhanced photocatalytic activity of these heterostructures.

Introduction

The design and controlled synthesis of heterogeneous nanostructures with well-defined morphologies is a significant frontier due to their multifunctional properties and new features arising from the effective couplings of their different domains.[1–8] The resulting nanocrystals can offer opportunities for the investigation of their facet-dependent catalytic, photocatalytic, molecular adsorption, and other surface-related properties. Recently, major advances in the synthesis and structural characterization of heterostructures have made in-depth investigation of the structure–property relationships of semiconductor–metal composites. There are a couple of important reasons why more than one phase, compound, or other constituent might be gainfully fused to make a composite material. For example, the surface chemical properties of a core particle can be modified by a second compound to provide colloidal stability or resistance to oxidation, or added functionality.[9–13] Here, however, we focus on the growth mechanism and the design and synthesis of heterostructures with desired morphology, selectivity, and activity. Up to now, several groups have synthesized very interesting heterostructures successfully. For example, Kuo *et al.* reported novel Au–Cu_2O core–shell heterostructures and showed the highly facet-dependent electrical properties of Cu_2O nanocubes and octahedra and significant enhancement by gold nanocrystal cores of the electrical conductivity of the octahedra.[8] Jin-Phillipp *et al.* studied the growth of one-dimensional fluorinated copper phthalocyanine ($CuPcF_{16}$) on Au nanoparticles and implied that the $CuPcF_{16}$ molecules nucleate at the ⟨110⟩ edge of the Au nanoparticle and grow parallel to a {111}facet of the particle along a direction

[a]Key Laboratory of Advanced Textile Materials and Manufacturing Technology, Zhejiang Sci-Tech University, Ministry of Education, Hangzhou 310018, P. R. China. E-mail: du@zstu.edu.cn; Tel: +86-571-86843255

[b]Department of Materials Engineering, College of Materials and Textile, Zhejiang Sci-Tech University, Hangzhou 310018, P. R. China

[c]MOE Key Laboratory of Macromolecular Synthesis and Functionalization, Department of Polymer Science and Engineering, Zhejiang University, Hangzhou 310027, China

† Electronic supplementary information (ESI) available. See DOI: 10.1039/c2ta00591c

close to {121}.[14] Mahmoud *et al.* prepared Cu_2O–Au nanoframes with different nanolayer thicknesses of Cu_2O and demonstrated an increase in the hole concentration, leading to an observed enhanced rate of dye degradation.[15] In these reports, due to the system energy minimization trend, the growth mainly took place only on facets and the surface-free-energy-distribution of the substrates could not be carefully studied, which may lead to unimaginable novel structures. However, the selective growth on specific positions of the substrates, especially only on the vertices, crystal edges and facets, *via* the direct assembly of atoms or ions remains challenging. This kind of selective growth of novel and complex structures with specific morphologies from nanocrystals is significant for the nanoscale adjustment and preparation of fascinating heterogeneous nanostructures.[16–20]

In this work, we report a novel strategy for the surface-free-energy-distribution induced selectively growth on specific positions such as vertices, crystal edges and facets, and construct a variety of Au nanostructures. In Torimoto's and Kitaev's strategies, selective growth on crystal edges was achieved by controlling the deposition rate and selectively capping the {100} facets, respectively.[21,22] In addition, in Fan's report, the selective etching by I_2 preferentially created highly active sites on the crystal edges or facets, which served as nucleation sites to direct the selective deposition and growth of Pt.[23] Here, however, we prepared a smooth substrate without any surfactants for the selective growth and it is believed that the vertices and crystal edges of the original structures possess actives sites (exposed high-index facets, defects, atom steps, and kinks), which can act as nucleation sites and induce the selective deposition and growth of Au.[1,2,24–27] The goal of this research is to understand the surface-free-energy-distribution of the substrate caused by defects and provide a fine structural feature that can be produced by selective deposition of other metals onto substrates.

As a perspective material with wide applications in photocatalysis, gas sensors, solar energy conversion, *etc.*, Cu_2O octahedra were introduced to use as the template for the selective growth of Au, which can result in enhanced properties of the composite materials.[28–33] In our previous work, AuNGs selectively grown on specific positions (tips, edges and facets) of Cu_2O octahedra are successfully obtained and these heterostructures show fascinating degradation of methylene blue.[34] For the present work, in order to ensure the structural integrity of the pristine template, we firstly studied the influence of the amounts of reducing agents and the reaction time in the synthesis of Cu_2O octahedra, and then obtained optimum octahedra for the selective growth. The Cu_2O octahedron possesses six vertices, twelve crystal edges and eight {111} facets, and due to the high density of low-coordinated atoms at the vertices and crystal edges, these structures can serve as active sites.[2,3,18,34–37] In our present work, four different morphologies of Cu_2O–Au hierarchical heterostructures are obtained by changing the amount of Au precursor. Meanwhile, to better understand the surface-free-energy-distribution induced selective growth of AuNGs, Cu_2O octahedra coated by PVP were taken as control to probe the influence of the surface energy distribution on the morphology of the products. Their chemical, morphological, and crystallographic properties were studied in detail by transmission electron microscopy (TEM), high resolution transmission electron microscopy (HRTEM), field emission scanning electron microscopy (FE-SEM), energy-dispersive X-ray spectrometry (EDS), X-ray photoelectron spectroscopy (XPS), and X-ray diffraction (XRD). Further elaborative studies are also provided to understand the growth mechanism of the surface-free-energy-distribution induced selective growth of AuNGs on Cu_2O octahedra. Moreover, the photocatalytic performances of the as-prepared Cu_2O and Cu_2O–Au hierarchical heterostructures for the degradation of methyl orange (MO) were investigated. It should be noted that these Cu_2O–Au hierarchical heterostructures show enhanced photocatalytic activity and the photo-induced charge separation in these heterostructures should be more efficient than in pure semiconductor nanocrystals, leading to an enhanced photocatalytic activity.

Experimental method

Materials

Anhydrous copper(II) chloride ($CuCl_2$) and hydrazine hydrate ($N_2H_4 \cdot 2H_2O$) were purchased from Aladdin Chemistry Co., Ltd. Chloroauric acid ($HAuCl_4 \cdot 4H2O$, 99.9%) was acquired from Shanghai Civi Chemical Technology Co., Ltd. Poly-(vinylpyrrolidone) (PVP, $K_{29\text{-}32}$) was purchased from Shanghai Chemical Reagent Co., Ltd. Methyl orange (MO) was purchased from Tianjin Yongda Chemical Reagent Co., Ltd. Absolute ethyl alcohol was bought from Hangzhou Gaojing Fine Chemical Co., Ltd. All the chemicals were used as received without further purification. Deionized water was used for all solution preparations.

Synthesis of various morphologies of Cu_2O nanocrystals

The Cu_2O nanocrystals with systematic shape evolution from cubic octahedral to corrosive-octahedral structures were synthesized through reduction of $CuCl_2$ by hydrazine hydrate. The sample beakers were placed on a magnetic stirrer at room temperature. 1 mL of 0.1 M $CuCl_2$ solution without any surfactant was added to each beaker with vigorous stirring. Then, 1 mL of 1.0 M NaOH solution was introduced. The resulting solution turned light blue immediately, indicating the formation of a $Cu(OH)_2$ precipitate. After the complete formation of the $Cu(OH)_2$ precipitate, 10, 40, 80, 120, 200 and 300 μL of $N_2H_4 \cdot 2H_2O$ were quickly injected in 3 s into the beakers by pipette. The total solution volume of each beaker is 30 mL. The solutions of each beaker were kept at room temperature for 10 min and then centrifuged at 5000 rpm for 5 min. The prepared Cu_2O nanocrystals with 10 μL $N_2H_4 \cdot 2H_2O$ added were kept on a magnetic stirrer for 5, 30 and 60 min for nanocrystal growth. All the as-prepared Cu_2O nanocrystals were centrifuged at 5000 rpm for 5 min and washed 3 times with 10 mL deionized water to remove the unreacted chemicals. The final washing step used 10 mL of ethanol, and the precipitate was dispersed in 4 mL ethanol for storage and the following characterizations.

Synthesis of Cu_2O–Au hierarchical heterostructures with various Au nanostructures

In the case of synthesis of Cu_2O–Au hierarchical heterostructures, the Cu_2O octahedral nanocrystals were firstly dissolved in 30 mL deionized water, and then, 0.00, 0.25, 0.50, 0.75 and 1.00 mL of 5 mM $HAuCl_4$ aqueous solution were respectively added to the samples and labeled a, b, c, d, and e. The typical yellow color of the $HAuCl_4$ aqueous solution and the brick-red of Cu_2O disappeared immediately. Instead, a certain amount of black product was formed. The product solutions were placed on a magnetic stirrer at room temperature with vigorous stirring for 3 h. For the synthesis of the Cu_2O–PVP–Au heterostructures, at the same conditions, PVP was introduced to study the selective growth of Au nanograins (AuNGs) on Cu_2O octahedral nanocrystals. 3 mL PVP solution (the mass fraction is 1%) was dropped into the Cu_2O octahedra solution (dissolved in 30 mL deionized water), and then 0.25, 0.5, 0.75 and 1 mL of 5 mM $HAuCl_4$ aqueous solution were respectively added to the samples. In addition, at the same conditions, 2.5 mL, 5 mL, 7.5 mL and 10 mL PVP solution (the mass fraction is 1%) were respectively added to the Cu_2O octahedra solution (dissolved in 30 mL deionized water). After 30 min for complete adsorption, 0.25 mL $HAuCl_4$ aqueous solution was added to each samples and the reaction time was 3 h for each sample. For 5 mL PVP coated Cu_2O octahedra, 0.10, 0.15, 0.20 and 0.25 mL $HAuCl_4$ were added into the solution, respectively. All the as-prepared Cu_2O–Au and Cu_2O–PVP–Au heterostructures with various structures were centrifuged at 5000 rpm for 5 min and washed 3 times with 20 mL deionized water to remove the unreacted chemicals. The final washing step used 10 mL of ethanol, and the precipitate was dispersed in 4 mL ethanol for storage and the following analysis.

Photocatalytic activity measurements

The evaluation of the samples for photocatalytic degradation of MO aqueous solution was performed at room temperature (25 °C). 4 mg of the prepared Cu_2O and Cu_2O–Au hierarchical heterostructure samples labeled a, b, c, d, and e were completely dispersed into 20 mL of MO aqueous solution (10^{-4} M), respectively. The suspension was magnetically stirred in the dark for 3 h to ensure absorption equilibrium of MO on the surface of the photocatalyst. A 500 W xenon lamp equipped with a UV cutoff filter ($\lambda > 400$ nm) and a congealed system, was used as the light source, which was about 15 cm away from the solution. After given time intervals, 5 mL solution was taken out and centrifuged to remove the photocatalyst for UV-Vis absorption measurements.

Instrumentation

Field emission scanning electron microscopy (FE-SEM) images of the synthesized Cu_2O and Cu_2O–Au hierarchical heterostructures were obtained using a JSM-6700F field-emission scanning electron microscope (JEOL, Japan). Transmission electron microscopy (TEM) characterization was performed on a JEOL JEM-2100 electron microscope operating at 200 kV. Powder X-ray diffraction (XRD) patterns were collected using a SIEMENS Diffraktometer D5000 X-ray diffractometer using a Cu Kα radiation source at 35 kV, with a scan rate of 0.02° 2θ s^{-1} in the 2θ range of 10–80°. X-ray photoelectron spectra of the Cu_2O octahedra and Cu_2O–Au heterostructures (0.25 mL $HAuCl_4$) were recorded by using an X-ray photoelectron spectrometer (XPS) (Kratos Axis Ultra DLD) with an aluminum (mono) Kα source (1486.6 eV). The aluminum Kα source was operated at 15 kV and 10 mA. UV-Vis absorption spectra were acquired with the use of a Lambda 900 UV-Vis spectrophotometer (Perkin Elmer, USA). All the spectra were collected over a wavelength range of 300–600 nm.

Results and discussion

In this part, we firstly studied the influence of the reductant for synthesizing the Cu_2O template and got an optimal Cu_2O morphology for the design of selective growth of AuNGs. The procedures used to synthesize Cu_2O nanocrystals and Cu_2O–Au heterostructures are illustrated in Scheme S1† and the amounts of all chemicals are shown in Table S1(see ESI†). As demonstrated in Fig. 1, clearly morphological evolutions are obtained through changing the amount of $N_2H_4 \cdot 2H_2O$. A small amount of $N_2H_4 \cdot 2H_2O$ of about 10 μL results in Cu_2O cuboctahedra, while octahedra are obtained with 40 and 80 μL $N_2H_4 \cdot 2H_2O$ added. As shown in Fig. 1a–c, there are some wire-like products, which are also Cu_2O nanocrystals.[38–41] When the amount of $N_2H_4 \cdot 2H_2O$ increases to 120 μL, Cu_2O octahedra with smooth facets and crystal edges are obtained, indicating that the wire-like Cu_2O nanocrystals completely evolve into Cu_2O octahedra. With the further increase of reductants, some holes emerge on the facets of the Cu_2O octahedra and the facets of Cu_2O become relatively rough and irregular. When the amount increases to 300 μL, the holes on the facets become much bigger and the structure of some octahedra are damaged. These phenomena are mainly due to portions of Cu_2O converting to Cu particles caused by the excess amount of strong reductants, which is in accordance with the literature.[39,42–44] In addition, an interesting result should be noted that the evolution of Cu_2O from

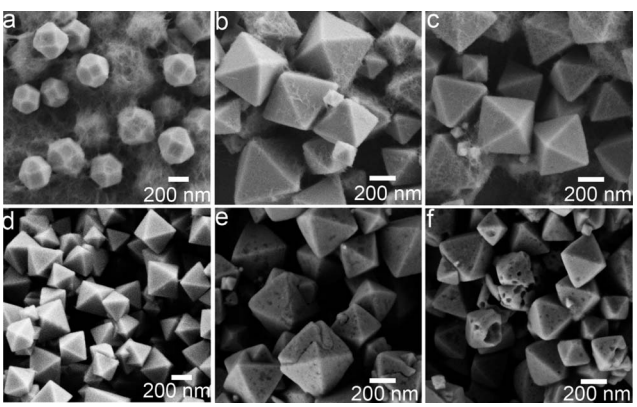

Fig. 1 FE-SEM images of the Cu_2O nanocrystals synthesized with morphological evolutions by using different amounts of $N_2H_4 \cdot 2H_2O$. (a) 10 μL, (b) 40 μL, (c) 80 μL, (d) 120 μL, (e) 200 μL, (f) 300 μL. The reaction time for each sample is 10 min.

cuboctahedron to octahedron is closely related to the reaction time with the same amount of $N_2H_4 \cdot 2H_2O$. As depicted in Fig. S1 (see ESI†), 10 μL $N_2H_4 \cdot 2H_2O$ was used to test the evolution, and with the reaction time increasing from 10 min to 60 min, the evolution from cuboctahedra to octahedra is observed, indicating that octahedra can also be obtained by changing the concentration of reductants or the reaction time. More discussion can be found in the ESI.†

As demonstrated in Fig. 2, cuboctahedra bounded by eight {111} facets and six {100} facets, octahedra and corroded octahedra bounded by eight {111} facets are provided. Comparing Fig. 2f with Fig. 2j, corroded octahedra lose their smooth surfaces and crystal edges, which are in agreement with the FE-SEM results. The SAED patterns match the respective orientations of the cuboctahedra, octahedra and corroded octahedra. The HRTEM images taken near the nanocrystal edges reveal distinct lattice fringes with *d* spacings of 2.9 and 2.4 Å, which correspond to the (110) and (111) lattice planes of Cu_2O. The lattice plane directions are also consistent with the respective crystal orientations. Based on the above characterizations, the Cu_2O octahedra with smooth crystal edges and facets prepared by 120 μL $N_2H_4 \cdot 2H_2O$ are used for the selective growth of AuNGs.

TEM and FE-SEM characterization were introduced to test the feasibility of the design of the surface-free-energy-distribution induced selective growth of AuNGs on Cu_2O octahedra. Fig. 3 shows different Cu_2O–Au hierarchical heterostructures with the morphological evolutions by increasing the amounts of $HAuCl_4$. As shown in Fig. 3a and e, crystal edges with quasi-1D shapes show higher levels of AuNG coverage due to the high surface free energy, while a few AuNGs exist on the {111} facets, indicating the preferential growth of AuNGs. The phenomenon of a few AuNGs on the facets is attributed to the overgrowth of AuNGs on crystal edges and the decreasing surface energy of the crystal edges, and then more and more AuNGs would start to form on the {111} facets. The AuNGs are comprised of a couple of small Au nanoparticles (AuNPs) with an average diameter of 5 nm, which is shown in Fig. S2 (see ESI†). The average diameter of the AuNGs is 28.1 ± 3.9 nm (Fig. S3, see ESI†). The crystal edges of the Cu_2O octahedra possess a relatively high aspect ratio and the increased surface area allows for greater feasibility of growth on defect lattice sites with higher surface free energies. Fig. 3b and f show that after the original preferential growth along the crystal edges, more and more AuNGs start to form on the {111} facets and these AuNGs begin to join together to form a solid facet. With the continuous increasing amount of $HAuCl_4$, the Cu_2O octahedra are completely encapsulated by a shell of irregularly arranged AuNGs, which are shown in Fig. 3c and g. Moreover, there are some pores and splits on the AuNGs shells, demonstrating that the AuNGs shells are fabricated by etching out Cu_2O portions, which can confirm the galvanic reaction between Cu_2O and $AuCl_4^-$. A higher magnification TEM image shows the etching Cu_2O octahedra, which is shown in Fig. S4. (see ESI†) When the amount of $HAuCl_4$ increases to 1.00 mL, with the porous structure of the AuNGs shells, $AuCl_4^-$ ions can diffuse into the shells and continuously reacted with the inner Cu_2O. From Fig. 3d and h, an interesting phenomenon is observed that a large amount of AuNWs ranging from 30 to 80 nm (Fig. S5†) are densely grown on the AuNG shells. The HRTEM and FFT images taken for four different Cu_2O–Au hierarchical heterostructures reveal distinct lattice fringes with *d* spacings of 2.3 Å, which corresponds to the (111) lattice planes of Au, indicating that the growth direction of AuNWs is along the ⟨111⟩ axes.[45,46]

To better understand the surface-free-energy-distribution induced selective growth of AuNGs, Cu_2O octahedra coated by a

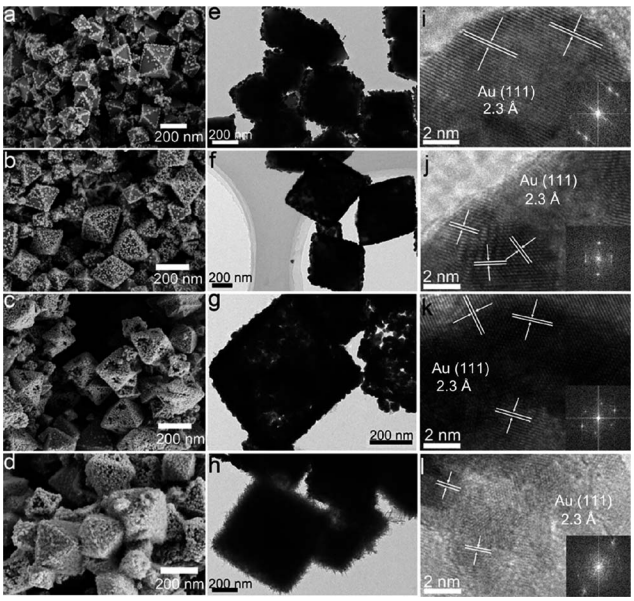

Fig. 3 FE-SEM images, TEM images of the surface energy induced selective growth of AuNGs on Cu_2O octahedra with increasing amounts of $HAuCl_4$: (a and e) 0.25 mL, (b and f) 0.50 mL, (c and g) 0.75 mL and (d and h) 1.00 mL. HRTEM images of the AuNGs (i, j and k) and AuNWs (l). The insets are the corresponding FFT images of AuNGs and AuNWs.

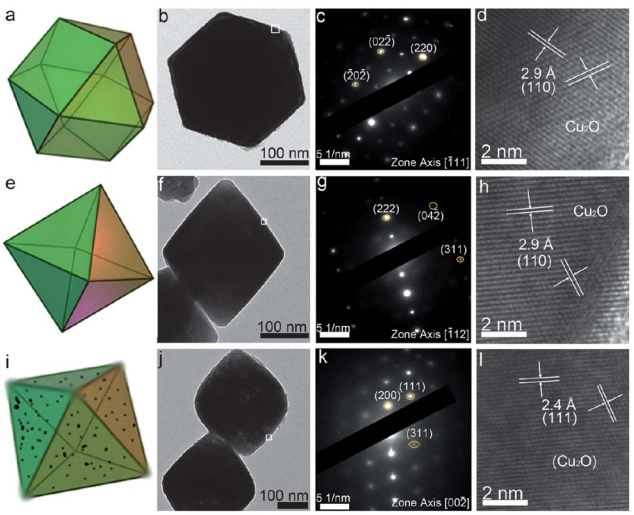

Fig. 2 Models, TEM images, selected area electron diffraction (SAED) patterns and HRTEM images of the square regions of (a–d) Cu_2O cuboctahedra, (e–h) octahedra, and (i–l) corroded octahedra viewed along the [100], [111], and [111] directions. The amounts of $N_2H_4 \cdot 2H_2O$ are 10 μL, 120 μL, and 200 μL, respectively.

certain amount of PVP were taken as control to probe the influence of surface energy distribution on the morphology of the products. It is commonly accepted that PVP adsorbs preferentially on specific positions on the surface with higher energy, and the surface free energy distribution can be changed.[23,47] Therefore, the adsorption of PVP molecules on the surface of Cu_2O octahedra would generally obey the energy order, that is PVP molecules firstly adsorb on crystal edges and then the {111} facets. In this case, the PVP in the solution is gradually adsorbed on vertices, crystal edges and {111} facets of Cu_2O octahedra until equilibrium is established. As a result, the vertices and crystal edges with higher energies were preferentially covered by PVP, which can decrease the surface energy diversity of Cu_2O among vertices, crystal edges and facets.[23,47,48] As shown in the samples (0.25 mL $HAuCl_4$) without and with PVP (Fig. 3a and 4a), clearly difference between the two figures could be found. In Fig. 3a, most of the AuNGs were grown on the vertices and crystal edges. Even a few AuNGs were found on the facets, which is attributed to the overgrowth of the crystal edges. However, in Fig. 4a, most of the AuNGs were dispersed on the surface of the octahedra relative evenly, not only on the crystal edges shown in Fig. 3a, indicating the effectiveness of PVP to decrease the difference of surface energy between facets and crystal edges. More FE-SEM images can be seen in Fig. S6 (see ESI†). When the amounts of $HAuCl_4$ are further increased to 0.5 mL, 0.75 mL and 1.00 mL, respectively, more and more AuNGs form on the surfaces of octahedra until the octahedra are completely encapsulated by AuNG shells. Compared with Fig. 3d and h, no AuNWs exist on the AuNG shells and because of the dense arrangement and aggregation of AuNGs, the outline of the Cu_2O octahedra become more blurred (Fig. 4d and h). The HRTEM and FFT images of AuNGs taken at different Cu_2O–Au heterostructures illustrate that the AuNGs are formed by conjugated small AuNPs. The lattice fringes in the AuNGs with values of about 2.3 Å are well matched with the (111) lattice planes of Au.

Based on the above results, the PVP molecules indeed affect the surface-free-energy-distribution of Cu_2O octahedra and then the selective growth of AuNGs. However, on the other hand, different amounts of $HAuCl_4$ may lead to different growth processes and a series of experiments were used to investigate the influence of PVP on the surface energy distribution of Cu_2O octahedra and the selective growth. To further test the effectiveness of the strategy for the surface-free-energy-distribution induced selective growth, a series of amounts of PVP were used to demonstrate the evolution of the surface energy distribution of the Cu_2O octahedra for the selective growth of AuNGs. As seen in Fig. 5a and 3a, the AuNGs preferentially grow on the vertices and crystal edges of Cu_2O octahedra without PVP, and only a few AuNGs were found on the facets. After decoration by PVP, as shown in Fig. 5b, the surface energies of vertices and crystal edges gradually decreased and most of the AuNGs grow on the facets instead of the crystal edges, indicating that the PVP can effective change the surface energy distribution of the Cu_2O octahedra. However, several Cu_2O octahedra's crystal edges are still covered by AuNGs, indicating that the amount of PVP is not sufficient to reduce the crystal edges' energy to the facets' level. From Fig. 5c, when the amount of PVP is increased

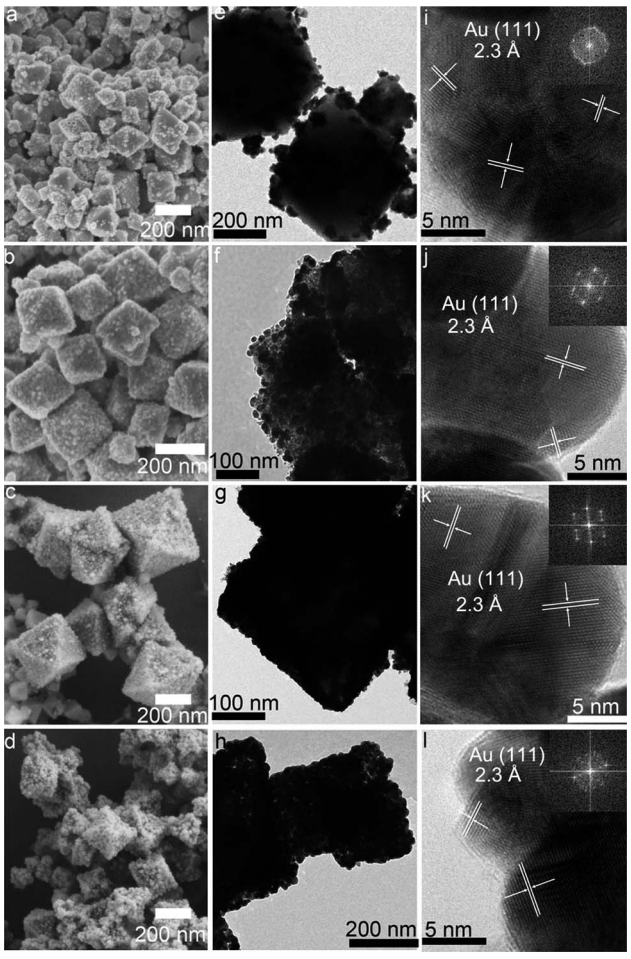

Fig. 4 FE-SEM images, TEM images of the Cu_2O–PVP–Au heterostructures with increasing amounts of $HAuCl_4$ in the presence of 0.20 M PVP: (a and e) 0.25 mL, (b and f) 0.50 mL, (c) 0.75 mL and (d and h) 1.00 mL. HRTEM images of the AuNGs (i, j, k and l). The insets are the corresponding FFT images of the AuNGs.

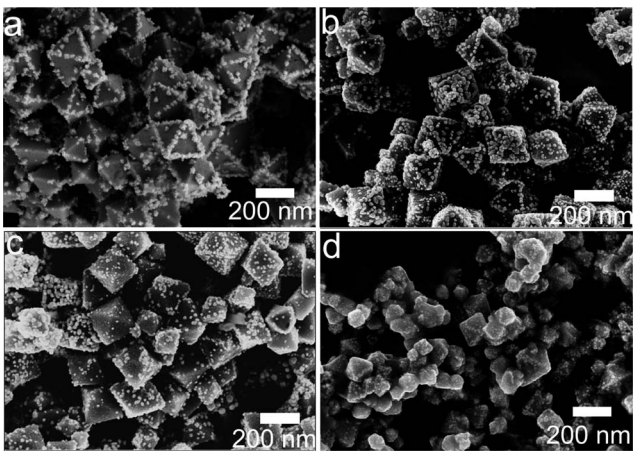

Fig. 5 FE-SEM images of Cu_2O–PVP–Au heterostructures with increasing amounts of PVP (0.20 M) in the presence of 0.25 mL $HAuCl_4$: (a) 0 mL, (b) 2.5 mL, (c) 5 mL and (d) 7.5 mL.

to 0.50 mL, most of the AuNGs are randomly dispersed on the surface of Cu_2O octahedra, indicating that the diversity of the surface energy distribution decreased. With the further increase to 7.5 mL, the Cu_2O octahedra were coated by a layer of PVP and a similar phenomenon was found for the sample with 5 mL added. Therefore, with the increasing absorption of PVP on Cu_2O octahedra, the diversity of the surface energy distribution decreased and the trend of selective growth of AuNGs also decreased.

Meanwhile, an appropriate amount of $HAuCl_4$ should be considerable for the selective growth of AuNGs, which is due to the higher surface energy of crystal edges than the {111} facets; the $AuCl_4^-$ at an appropriate concentration can be preferentially absorbed on crystal edges and reduced by Cu(I) sites, forming AuNPs. However, when a larger amount of $AuCl_4^-$ was promptly introduced into the colloid solution, the preferential adsorption and reduction of $AuCl_4^-$ on the crystal edges became undistinguished because active sites on both the (111) and (100) planes are completely occupied by $AuCl_4^-$. To further clarify the surface-free-energy-distribution induced selective growth of AuNGs, a much lower concentration of $HAuCl_4$ was used to demonstrate the growth of the AuNGs on the Cu_2O octahedra surfaces with PVP. In the present experiment, the Cu_2O templates were firstly decorated by 5 mL PVP, and then, 0.10, 0.15, 0.20 and 0.25 mL $HAuCl_4$ were added into the PVP-coated Cu_2O octahedra solution, respectively. Fig. 6a shows that the AuNGs grow both on the crystal edges and {111} facets, and the number of AuNGs on the crystal edges is a little more than on the facets, indicating that the surface energy of the crystal edges is still higher than that of the {111} facets. However, comparing Fig. 3a with 5a, the amount of AuNGs growing along the crystal edges is significantly decreased, indicating the decrease of the diversity of the surface energy distribution between crystal edges and {111} faces. With the increasing amount of $HAuCl_4$, from Fig. 6b–6d, the number of AuNGs growing both on facets and crystal edges increased and the trend of the disordered dispersion of AuNGs is not changed. Consequently, it can be seen that PVP can effective reduce the diversity of the surface-free-energy-distribution of the Cu_2O surface between vertices and crystal edges, resulting in the amount of selective growth of AuNGs decreasing. In conclusion, through all the above results, the surface-free-energy-distribution can induce the selective growth of AuNGs and form Cu_2O–Au hierarchical heterostructures with a series of morphological evolutions.

The identity and crystal phase structures of these Cu_2O, Cu_2O–Au and Cu_2O–PVP–Au nanocrystals are manifested through XRD characterization. As shown in Fig. 7A, all the diffraction peaks located at 29.55°, 36.42°, 42.30°, 61.34° and 73.53° can be indexed as Cu_2O nanocrystals (JCPDS:05-0677), and no other impurity peaks could be detected, indicating the pure phase of the Cu_2O nanocrystals.[49–51] Although their XRD patterns look similar, close examination shows that the intensity of the (110) peak, (200) peak, (220) peak and (311) peak decrease with increasing volumes of $N_2H_4 \cdot 2H_2O$ (from curve a to curve d). It is conjectured that with the increasing volumes of reducing agent, the corrosions in some facets of the Cu_2O nanocrystals become more severe, resulting in the low intensity of diffraction peaks, which are in agreement with the FE-SEM and TEM images (Fig. 1 and 2). Fig. 7B and C show XRD patterns of the Cu_2O–Au hierarchical heterostructures and Cu_2O–PVP–Au heterostructures, suggesting that the products consist of both Cu_2O and Au crystals. The new emerging diffraction peaks located at 38.19°, 44.39°, 64.58° and 81.72° can be indexed to the Au crystal (JCPDS: 65-2870), which correspond to the (111), (200), (220) and (311) planes of face-center cubic (fcc) gold, indicating that AuNGs were successfully formed, that is, $AuCl_4^-$ can be spontaneously reduced onto the surfaces of Cu_2O without additional reductive agents at room temperature.[52–55]

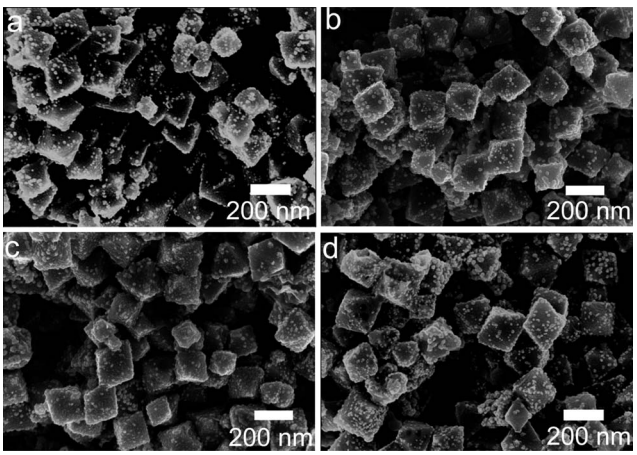

Fig. 6 FE-SEM images of Cu_2O–PVP–Au heterostructures with increasing amounts of $HAuCl_4$ in the presence of 5 mL of PVP (0.20 M): (a) 0.10 mL, (b) 0.15 mL, (c) 0.20 mL and (d) 0.25 mL.

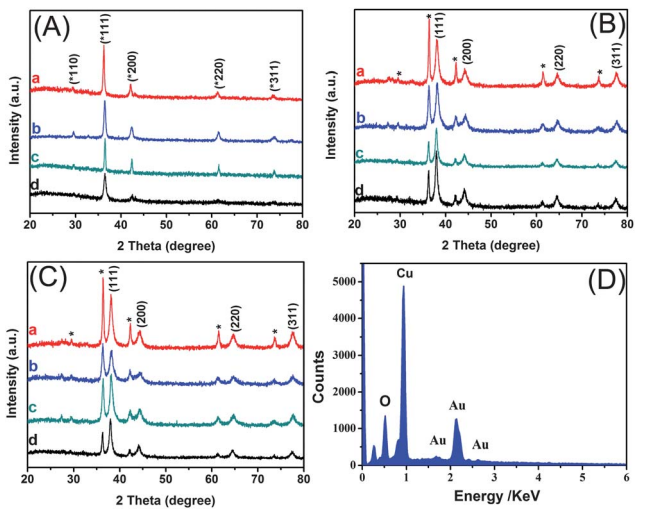

Fig. 7 (A) XRD patterns of the as-synthesized Cu_2O nanocrystals with different amounts of $N_2H_4 \cdot 2H_2O$, (a) 10 μL, (b) 120 μL, (c) 200 μL and (d) 300 μL. (B) XRD patterns of the as-prepared Cu_2O–Au hierarchical heterostructures with various volumes of $HAuCl_4$ (5 mM), (a) 0.25 mL, (b) 0.5 mL, (c) 0.75 mL and (d) 1 mL. (C) XRD patterns of the obtained Cu_2O–PVP–Au heterostructures with various volumes of $HAuCl_4$ (5 mM), (a) 0.25 mL, (b) 0.5 mL, (c) 0.75 mL and (d) 1 mL. (D) EDS spectrum of Cu_2O–Au hierarchical heterostructures (0.5 mL $HAuCl_4$). The peaks of the Cu_2O nanocrystals are labeled with *.

Comparing Fig. 6b and c, close examination shows that the ratio of the intensity of the (111) peak of Au to that of the (*111) peak of Cu_2O increases with increasing amounts of $HAuCl_4$. This trend is attributed to the continuous growth of AuNGs on Cu_2O nanocrystals and, in addition, it is speculated that the decrease of the intensity of Cu_2O nanocrystal peaks are mainly caused by the etching of Cu_2O during the transformation process (Fig. S4†).

XPS was further used to probe the surface chemical compositions and chemical oxidation state of the as-prepared Cu_2O octahedra and AuNWs grown on the Cu_2O octahedra (Fig. 8). The XPS spectra from 958 to 928 eV shown in Fig. 8A and B demonstrate the photoelectron spectrum of the Cu 2p core level for the Cu_2O octahedra and Cu_2O–Au heterostructures (1.00 mL $HAuCl_4$). The binding energies obtained in XPS analysis were corrected for specimen charging by referencing the C 1s to 283.20 eV. As shown in Fig. 8A, there are two main Cu 2p XPS peaks at 933.2 and 953.1 eV, which could be attributed to the Cu^+ double peaks for Cu $2p_{3/2}$ and Cu $2p_{1/2}$ respectively.[56–58] This confirms that the main composition of the structure is Cu_2O. The satellite peak at 941.6 eV located at higher binding energy than that of the main Cu $2p_{3/2}$ peak is typically associated with copper in the bivalent binding energy state, which can be assigned to Cu^{2+} in CuO or probably $Cu(OH)_2$ species.[56–59] The relatively low peak implies a small amount of $Cu(OH)_2$ or CuO on the surface of the Cu_2O. The Cu LMM Auger peaks' kinetic energy of the Cu_2O octahedra before and after the growth of AuNWs are located at 569.0 and 567.8 eV, respectively, demonstrating that their surfaces remain Cu_2O (Fig. S7, see ESI†).[60,61] After galvanic reaction with $AuCl_4^-$, the binding energies of the Cu^+ double peaks for Cu $2p_{3/2}$ and Cu $2p_{1/2}$ move to 932.4 and 952.4 eV, respectively, indicating the binding of surface Cu atoms in the Cu_2O–Au heterostructures with the surrounding AuNGs and AuNWs, which leads to substantial electron donation from Cu_2O to the surroundings.[45,60,61]

From Fig. 8B, the new emerging peaks located at 940.3 eV can be attributed to the Cu^{2+} binding energy, which is caused by the galvanic reaction between Cu_2O and $AuCl_4^-$. In addition, the intensity of Cu^{2+} become relatively strong after the growth of AuNGs and AuNWs, implying the conversion from Cu^+ to Cu^{2+} during the galvanic reaction. The O 1s XPS spectra shown in Fig. 6c also provide more information about the galvanic reaction. The peaks located at 530.7 and 529.4 eV are both ascribed to O^{2-} ions in Cu_2O octahedra.[56–60,62,63] The binding energy shift of O 1s from 530.7 eV to 529.4 eV in Cu_2O before and after galvanic reaction was a result of the strong coordination between AuNGs and oxygen, which can be seen in Fig. 3d and h. Fig. 8D show the XPS spectrum in the Au 4f region of the Cu_2O–Au heterostructures. It can be seen from the spectrum that the two XPS peaks at 81.9 eV and 85.6 eV are in agreement with the binding energies of Au $4f_{7/2}$ and Au $4f_{5/2}$, respectively.[43] The above information provides more details about the galvanic reaction and confirms that the Cu_2O–Au hierarchical heterostructures have been prepared successfully.

Further elaborative studies are contemplated to understand the mechanism of the surface-energy-distribution induced selective growth of AuNGs on Cu_2O octahedra with morphological evolutions. TEM images of the process of growth of the AuNGs selectively grown on different positions of Cu_2O octahedra are shown in Fig. 9 and the present selective growth process is schematically illustrated in Scheme 1. In Fan's reports,[23] KI solution was introduced to selectively etch the crystal edges of Au polyhedrons to create active sites (exposed high-index facets, defects, atom steps, and kinks) for the selective growth of Pt structures. They believed that the positions with high surface free energy act as nucleation sites to induce selective growth along specific orientations, which leads to the formation of regularly shaped NPs. Meanwhile, another group had reported that platinum grows on the planar faces of

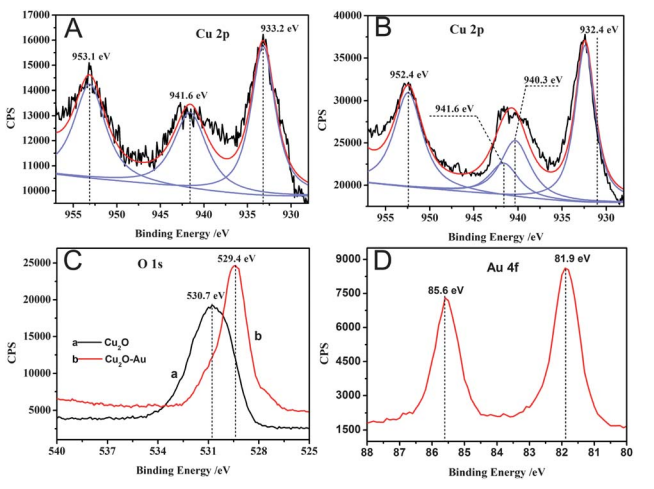

Fig. 8 Cu 2p XPS spectra of (A) Cu_2O octahedra and (B) Cu_2O–Au heterostructures (1.00 mL $HAuCl_4$). (C) O 1s XPS spectra of (a) Cu_2O octahedra and (b) Cu_2O–Au heterostructures (1.00 mL $HAuCl_4$). (D) Au 4f XPS spectrum of Cu_2O–Au heterostructures (1.00 mL $HAuCl_4$).

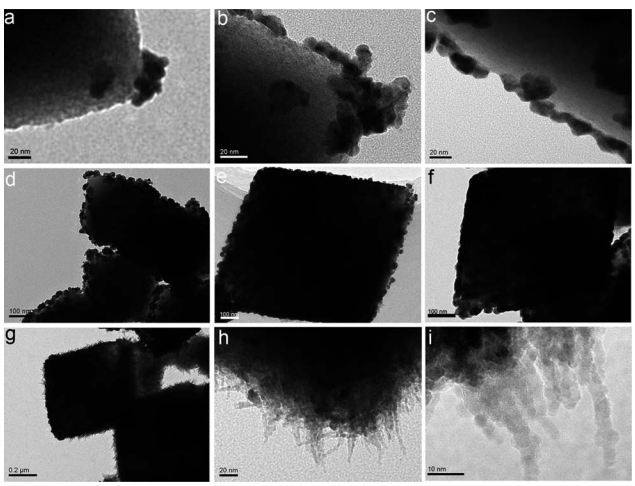

Fig. 9 TEM images of the growth process of the surface-free-energy-distribution induced AuNGs selectively grown on different positions of Cu_2O octahedra by adopting a series of amounts of $HAuCl_4$. (a) 0.10 mL, (b) 0.15 mL, (c) 0.20 mL, (d) 0.25 mL, (e) 0.50 mL, (f) 0.75 mL, and (g) 1.00 mL. (h–i) Higher-magnification TEM images of the AuNWs.

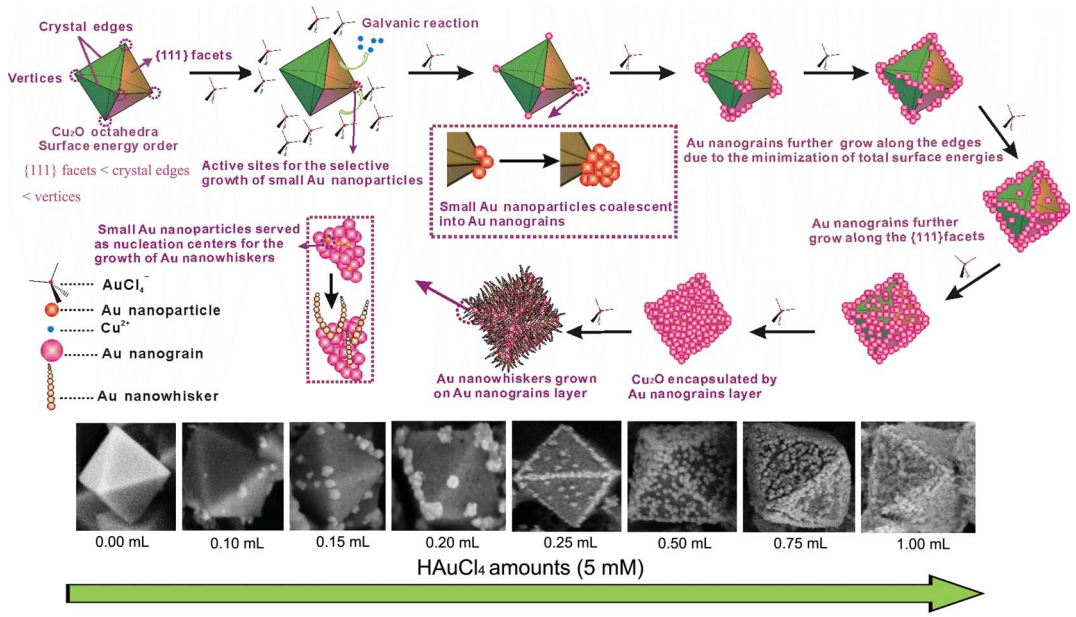

Scheme 1 Schematic illustration of the surface-free-energy-distribution induced selective growth of AuNGs on Cu_2O octahedra with morphological evolutions.

gold cubes, while the overgrowth occurred at the vertices of gold octahedra, indicating that platinum was selectively reduced on the Au (100) surface for each gold nanocrystal shape.[64] They also pointed out the key for the selective growth was the surface structures and energy distributions. However, the templates used for the selective growth were generally coated with some surfactants, which may affect the surface energy distribution of the original surface structures. Therefore, in the present work, Cu_2O templates synthesized without any surfactants were used for the selective growth to test whether AuNGs can grow on specific positions, because of the diversity of the surface energy distribution of the original surface structures. As demonstrated in Fig. 9a, the AuNGs are preferential formed on the vertices of the octahedra due to the relatively high surface energy. From a crystallographic point of view, different exposed facets have characteristic surface properties because of differences in atomic arrangement, lattice symmetry, and spacing. This fact has been applied to upgrade the shape-dependent reaction selectivity in catalysis.[2,3] It is well known that high-index facets hold much more surface defects and steps and kink atoms with low coordination numbers, and therefore, surface atoms located on the vertices and crystal edges are usually active sites for many reactions.[2–4,14,65] In addition, surface energies play a critical role in determining the shape of nanocrystals and for metals, such as copper oxide, which crystallizes in a face cubic centered (fcc) structure, theoretical studies reported that the {111} facets are the most densely packed surface and have the smallest surface free energy.[2–4] In fact, this quasi-spherical morphology minimizes the total energy by combining a small surface area with facets exhibiting low surface energies.[65] As we know, the Cu_2O octahedron possesses six vertices, twelve crystal edges and eight {111} facets, and due to the high density of low-coordinated atoms at the vertices and crystal edges, these structures can serve as active sites. On the contrary, the {111} facets are atomic-scale flat with a closely packed surface, exhibiting the lowest surface energy, and the surface energy of octahedra generally follows the order of {111} facets < crystal edges < vertices.[2–4,23,65] Therefore, the diversity of the surface energy distribution of Cu_2O octahedra would lead to the selective growth of AuNGs at specific positions of the Cu_2O octahedra such as vertices, crystal edges and {111} facets.

Through galvanic displacement reaction, the $AuCl_4^-$ ions can be reduced on the Cu_2O octahedra due to the standard reduction potential different between $AuCl_4^-$/Au (0.99 V *vs.* SHE) and Cu^{2+}/Cu_2O (0.203 V *vs.* SHE) pairs; that is, $AuCl_4^-$ added into the Cu_2O colloid solution can be immediately reduced by Cu_2O at room temperature.[11,30,66] Therefore, because of the high activity of the vertices of the Cu_2O octahedra, the $AuCl_4^-$ ions at an appropriate concentration can be preferentially adsorbed on vertices, and converted into Au nuclei through galvanic reaction.[11,30] More and more Au nuclei grew into small AuNPs and these small AuNPs coalesced into AuNGs with an average diameter of 28.1 ± 3.9 nm (Fig. S3, see ESI†). In the selective growth process, these vertices and crystal edges with twin crystals of the Cu_2O octahedra are preferentially covered to minimize total surface energies. Therefore, with the continuous formation of AuNGs on vertices, the surface free energy of the vertices would drop down to the same level as the crystal edges. After that, the newly formed AuNGs began to grow along the crystal edges, resulting in the continuous decreasing of surface free energy, which can be seen in Fig. 9b and c and Scheme 1. When the crystal edges were overgrown by AuNGs (Fig. 9d), the surface energy of the crystal edges decreased to the same level as the {111} facets, resulting in the continuous growth of AuNGs on the {111} facets. From Fig. 9e and f and Scheme 1, the AuNGs were random grown on the {111} facets until the octahedra were completely covered by AuNG shells. As the amount of $HAuCl_4$ increases further, from Fig. 9g, an

interesting phenomenon is observed that a large amount of AuNWs were grown on the AuNG shells. In this case, the previously formed AuNGs are coalesced by small AuNPs and these small AuNPs can serve as primary active sites for the nucleation of AuNWs and crystal growth. As previously reported, if, during crystal growth, the added metal atoms continue with the same crystal structure as the seed, then it is an epitaxial process.[2–4,35,36] It is generally accepted that the coordination reagent kinetically controls the growth of the wire-like morphologies of metal nanostructures by selective adsorption and desorption on specific crystal surfaces.[48] The HRTEM images of AuNPs and AuNWs shown in Fig. 3k and l indicate the (111) lattice planes of the AuNPs and AuNWs, demonstrating that the seed AuNPs have the same chemical identity as the growth atoms. In addition, in the catalysis of the small AuNPs, the newly formed Au nuclei of the AuNWs continuously grew aligned along the growth direction of the ⟨111⟩ axes to form AuNWs.

In the PVP coated Cu_2O case, because of a need to minimize the total surface free energy, the PVP molecules were adsorbed on the surface of the Cu_2O octahedra, resulting in the homogenization of surface energies among the vertices, crystal edges and {111} facets. Therefore, the trend of the surface free energy induced selective growth of AuNGs decreased and the AuNGs were randomly grown on the surfaces of Cu_2O octahedra, which can be seen in Fig. 4, 5 and 6. Through all the above evidence and discussion, it is believed that the evolution of Cu_2O–Au hierarchical heterostructures involves four main steps: (1) the selective adsorptions of $AuCl_4^-$ on vertices; (2) the *in situ* formation of Au nuclei through galvanic reaction and the selective growth of AuNGs on the vertices; (3) the change of selective growth route from along the crystal edges to along the {111} facets; (4) the formation of AuNWs.

The successful preparation of Cu_2O–Au hierarchical heterostructures offers the opportunity to extend the photocatalytic activity investigation of semiconductor–metal materials. As previously reported,[67–72] a major challenge of semiconductor's photocatalytic performance is the undesirable process of electron–hole recombination. Through controllably depositing metal nanoparticles onto semiconductors, a Schottky barrier can be created at the semiconductor–metal junction, leading to the continuous transfer of electrons from semiconductor to metal nanoparticles until the equilibrium of the Fermi energy levels is achieved.[53,71] In a controlled photocatalytic experiment, we investigated the photocatalytic performance of Cu_2O and Cu_2O–Au hierarchical heterostructures toward the degradation methyl orange (MO).

For comparison, the photocatalytic activity of the Cu_2O octahedra and Cu_2O–Au hierarchical heterostructures, labeled with a, b, c, d and e, respectively, were analyzed. Fig. 10A shows the degradation plots of MO with different photocatalysts after visible light irradiation for 2 h. The corresponding UV-Vis absorption spectra are available in Fig. S8 (see ESI†). As shown in Fig. 10B, about 29%, 69%, 76%, 71%, and 91% of MO is photodegraded by the octahedra, AuNGs selectively grown along the crystal edges, AuNGs grown along the crystal edges and {111} facets, octahedra encapsulated by AuNGs shells and

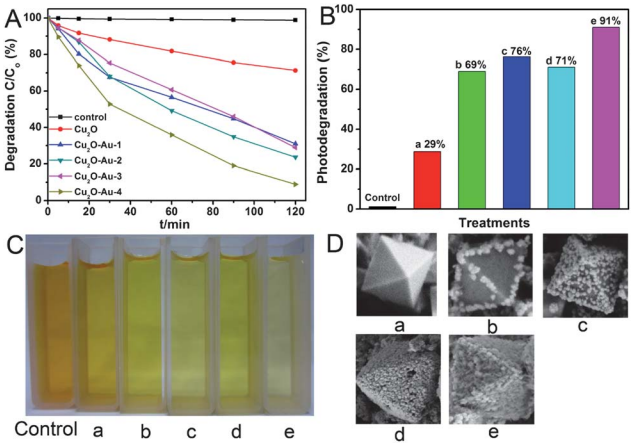

Fig. 10 (A) Degradation plots of MO with different photocatalysts: (control) without any photocatalyst; (a) Cu_2O octahedra; Cu_2O reacted with (b) 0.25 mL, (c) 0.50 mL, (d) 0.75 mL and (e) 1.00 mL $HAuCl_4$, respectively. (B) Percentage photodegradation of MO expressed as a reduction in the intensity of absorbance at 464 nm. (C) Photographs of the MO solution after irradiation for 2 h. (D) FE-SEM images of the corresponding photocatalysts.

AuNWs grown on AuNGs shells, respectively. Almost no photodegradation of MO was found for the blank sample without Cu_2O photocatalyst. These indicate that the photodegradation is caused by the Cu_2O and the photocatalytic activity of the Cu_2O and Cu_2O–Au hierarchical heterostructures follow the resultant order: AuNWs grown on AuNG shells (label e) > AuNGs grown along the crystal edges and {111} facets (label c) > octahedra encapsulated by AuNG shells (label d) > AuNGs selectively grown along the crystal edges (label c) > octahedra (label b). The color changes of the photodegraded solutions are shown in Fig. 10C. Notably, introducing Au into the composite material to form Cu_2O–Au cocatalysts resulted in a dramatic improvement in the photocatalytic performance due to the electron–hole recombination being suppressed. However, the photocatalytic activities of the Cu_2O–Au hierarchical heterostructures were not improved with the increasing loading amount of Au. The reduced photoactivity may be partially attributable to relatively higher Au loading in this system, which might decrease the total effective Cu_2O surface area during the photocatalytic degradation of MO. However, the AuNWs resulted in about 91% photodegradation of MO with the highest Au loading. The AuNWs ranging from 30 to 80 nm in length can provide more active surface area and it can offset the negative effects of photocatalytic activity caused by higher Au loading.

Conclusions

In summary, we have reported a novel strategy of surface-free-energy-distribution induced selective growth of AuNGs on specific positions of Cu_2O octahedra templates with a series of morphological evolutions from AuNG preferential growth on vertices, crystal edges and {111} facets, Cu_2O–Au core–shell nanostructures, and Au nanowhisker growth on AuNG shells. We firstly investigated the influence of reductant on the morphology and surface structures of the Cu_2O template to get

the optimum template with smooth surface and structural integrity. The surface energy distribution of the octahedra generally follows the order of {111} facets < crystal edges < vertices, leading to the selective growth of AuNGs on specific positions. TEM, HRTEM and FE-SEM investigate the morphological evolutions and crystal structures of Cu_2O and Cu_2O–Au hierarchical heterostructures. Meanwhile, Cu_2O octahedra coated by different amounts of PVP were taken as control and the results suggest that the trend of the selective growth on PVP coated Cu_2O octahedra decreased significantly because of the reducing diversity of the surface-free-energy-distribution. The identity and crystal phase structures of these Cu_2O, Cu_2O–Au and Cu_2O–PVP–Au nanocrystals are manifested through XRD and EDS. XPS further probes the surface chemical compositions and chemical oxidation state of the as-prepared Cu_2O and Cu_2O–Au hierarchical heterostructures to test the galvanic reaction between Cu_2O and $AuCl_4^-$. The growth mechanism of the surface-free-energy-distribution induced selective growth is also discussed. Moreover, the photocatalytic performances of the as-prepared Cu_2O and Cu_2O–Au hierarchical heterostructures for the degradation of methyl orange (MO) were investigated. These Cu_2O–Au hierarchical heterostructures show enhanced photocatalytic activity and the photo-induced charge separation in these heterostructures should be more efficient than in pure semiconductor nanocrystals, leading to enhanced photocatalytic activity.

Acknowledgements

We acknowledge the support of the project of the National Natural Science Foundation of China (NSFC) (Grant number: 50903072, 51243001), Zhejiang Province Natural Science Foundation (Grant number: Y4100197) and Science Foundation of Zhejiang Sci-Tech University (ZSTU) under no. 0901803-Y.

Notes and references

1 S. D. Sun, C. C. Kong, H. J. You, X. P. Song, B. J. Ding and Z. M. Yang, *CrystEngComm*, 2012, **14**, 40–43.
2 Z. W. Quan, Y. X. Wang and J. Y. Fang, *Acc. Chem. Res.*, 2012, DOI: 10.1021/ar200293n.
3 K. B. Zhou and Y. D. Li, *Angew. Chem., Int. Ed.*, 2012, **51**, 602–613.
4 T. He, X. Y. Zhang, J. Jia, Y. X. Li and X. T. Tao, *Adv. Mater.*, 2012, **24**, 2171–2175.
5 R. Costi, A. E. Saunders and U. Banin, *Angew. Chem., Int. Ed.*, 2010, **49**, 2–22.
6 H. Goesmann and C. Feldmann, *Angew. Chem., Int. Ed.*, 2010, **49**, 2–36.
7 Y. W. Jun, J. S. Choi and J. W. Cheon, *Angew. Chem., Int. Ed.*, 2006, **45**, 3414–3439.
8 C. H. Kuo, Y. C. Yang, S. J. Gwo and M. H. Huang, *J. Am. Chem. Soc.*, 2011, **133**, 1052–1057.
9 X. Wang, J. Zhuang, Q. Peng and Y. D. Li, *Nature*, 2005, **437**, 121–124.
10 E. Shaviv, O. Schubert, M. Alves-Santos, G. Goldoni, R. D. Felice, F. Vallee, N. D. Fatti, U. Banin and C. Sonnichsen, *ACS Nano*, 2011, **5**, 4712–4719.
11 X. W. Liu, *Langmuir*, 2011, **27**, 9100–9104.
12 Y. W. Jung, D. K. Ko and R. Agarwal, *Nano Lett.*, 2007, **7**, 264–268.
13 P. V. Kamat, *J. Phys. Chem. Lett.*, 2012, **3**, 663–672.
14 N. Y. Jin-Phillipp, T. N. Krauss and P. A. V. Aken, *ACS Nano*, 2012, **6**, 4039–4044.
15 M. A. Mahmoud, W. Qian and M. A. El-Sayed, *Nano Lett.*, 2011, **11**, 3285–3289.
16 M. Achermann, *J. Phys. Chem. Lett.*, 2010, **1**, 2837–2843.
17 P. D. Yang and J. M. Tarascon, *Nat. Mater.*, 2012, **11**, 560–563.
18 Z. K. Wu, *Angew. Chem., Int. Ed.*, 2012, **51**, 2934–2938.
19 A. Umemura, S. Diring, S. Furukawa, H. Uehara, T. Tsuruoka and S. Kitagawa, *J. Am. Chem. Soc.*, 2011, **133**, 15506–15513.
20 L. Z. Zhang, Z. H. Cheng, Q. Huan, X. B. He, X. Lin, L. Gao, Z. T. Deng, N. Jiang, Q. Liu, X. S. Du, H. M. Guo and H. J. Gao, *J. Phys. Chem. C*, 2011, **115**, 10791–10796.
21 M. McEachran, D. Keogh, B. Pietrobon, N. Cathcart, I. Gourevich, N. Coombs and V. Kitaev, *J. Am. Chem. Soc.*, 2011, **133**, 8066–8069.
22 K. Okazaki, J. Yasui and T. Torimoto, *Chem. Commun.*, 2009, 2917–2919.
23 N. N. Fan, Y. Yang, W. F. Wang, L. J. Zhang, W. Chen, C. Zou and S. M. Huang, *ACS Nano*, 2012, **6**, 4072–4082.
24 W. C. Wang, L. M. Lyu and M. H. Huang, *Chem. Mater.*, 2011, **23**, 2677–2684.
25 A. Dhakshinamoorthy and H. Garcia, *Chem. Soc. Rev.*, 2012, **41**, 5262.
26 W. C. Hou, L. Y. Chen, W. C. Tang and F. C. N. Hong, *Cryst. Growth Des.*, 2011, **11**, 990–994.
27 X. Wang and Y. D. Li, *J. Am. Chem. Soc.*, 2002, **124**, 2880–2881.
28 L. Zhang, H. Jing, G. Boisvert, J. Z. He and H. Wang, *ACS Nano*, 2012, **6**, 3514–3527.
29 S. Lee, C. W. Liang and L. W. Martin, *ACS Nano*, 2011, **5**, 3736–3743.
30 Y. Qin, R. C. Che, C. Y. Liang, J. Zhang and Z. W. Wen, *J. Mater. Chem.*, 2011, **21**, 3960–3965.
31 X. W. Liu, *RSC Adv.*, 2011, **1**, 1119–1125.
32 S. Chen, H. Y. Zhang, L. Y. Wu, Y. F. Zhao, C. L. Huang, M. F. Ge and Z. M. Liu, *J. Mater. Chem.*, 2012, **22**, 9117–9122.
33 K. X. Yao, X. M. Yin, T. H. Wang and H. C. Zeng, *J. Am. Chem. Soc.*, 2010, **132**, 6131–6144.
34 H. Zhu, M. L. Du, D. L. Yu, Y. Wang, M. L. Zou, C. S. Xu and Y. Q. Fu, *Dalton Trans.*, 2012, **41**, 13795.
35 Y. N. Xia, Y. J. Xiong, B. K. Lim and S. E. Skrabalak, *Angew. Chem., Int. Ed.*, 2009, **48**, 60–103.
36 Y. J. Xiong and Y. N. Xia, *Adv. Mater.*, 2007, **19**, 3385–3391.
37 R. Y. Zhang, A. Khalizov, L. Wang, M. Hu and W. Xu, *Chem. Rev.*, 2012, **112**, 1957–2011.
38 W. W. Huang, L. M. Lyu, Y. C. Yang and M. H. Huang, *J. Am. Chem. Soc.*, 2012, **134**, 1261–1267.
39 Y. Xu, H. Wang, Y. F. Yu, L. Tian, W. W. Zhao and B. Zhang, *J. Phys. Chem. C*, 2011, **115**, 15288–15296.
40 J. T. Zhang, J. F. Liu, Q. Peng, X. Wang and Y. D. Li, *Chem. Mater.*, 2006, **18**, 867–871.
41 Y. S. Luo, S. Q. Li, Q. F. Ren, J. P. Liu, L. L. Xing, Y. Wang, Y. Yu, Z. J. Jia and J. L. Li, *Cryst. Growth Des.*, 2007, **7**, 87–92.

42 H. L. Xu, W. Z. Wang and W. Zhu, *J. Phys. Chem. B*, 2006, **110**, 13829–13834.
43 F. Yang, Y. M. Choi, P. Liu, J. Hrbek and J. A. Rodriguez, *J. Phys. Chem. C*, 2010, **114**, 17042–17050.
44 Z. H. Wang, H. Wang, L. L. Wang and L. Pan, *Cryst. Res. Technol.*, 2009, **44**, 624–628.
45 H. Zhu, M. L. Du, M. L. Zou, C. S. Xu, N. Li and Y. Q. Fu, *J. Mater. Chem.*, 2012, **22**, 9301–9307.
46 C. G. Read, E. M. P. Steinmiller and K. S. Choi, *J. Am. Chem. Soc.*, 2009, **131**, 12040–12041.
47 S. M. Na and A. B. Flatau, *Smart Mater. Struct.*, 2012, **21**, 055024–055033.
48 X. Hong, G. Z. Wang, W. Zhu, X. S. Shen and Y. Wang, *J. Phys. Chem. C*, 2009, **113**, 14172–14175.
49 L. Zhang, D. A. Blom and H. Wang, *Chem. Mater.*, 2011, **23**, 4587–4598.
50 C. H. Kuo, T. E. Hua and M. H. Huang, *J. Am. Chem. Soc.*, 2009, **131**, 17871–17878.
51 H. T. Zhu, J. X. Wang and G. Y. Xu, *Cryst. Growth Des.*, 2009, **9**, 633–638.
52 H. Zhu, M. L. Du, M. L. Zou, C. S. Xu and Y. Q. Fu, *Dalton Trans.*, 2012, **41**, 10465–10471.
53 A. Pearson, H. Jani, K. Kalantar-zadeh, S. K. Bhargava and V. Bansa, *Langmuir*, 2011, **27**, 6661–6667.
54 X. Y. Liu, A. Q. Wang, X. D. Wang, C. Y. Mou and T. Zhang, *Chem. Commun.*, 2008, 3187–3189.
55 V. Vongsavat, B. M. Vittur, W. W. Bryan, J. H. Kim and T. R. Lee, *ACS Appl. Mater. Interfaces*, 2011, **3**, 3616–3624.
56 Z. H. Ai, L. Z. Zhang, S. C. Lee and W. K. Ho, *J. Phys. Chem. C*, 2009, **113**, 20896–20902.
57 Q. Hua, D. L. Shang, W. H. Zhang, K. Chen, S. J. Chang, Y. S. Ma, Z. Q. Jiang, J. L. Yang and W. X. Huang, *Langmuir*, 2011, **27**, 665–671.
58 J. H. Zhong, G. R. Li, Z. L. Wang, Y. N. Ou and Y. X. Tong, *Inorg. Chem.*, 2011, **50**, 757–763.
59 Q. Hua, K. Chen, S. J. Chang, Y. S. Ma and W. X. Huang, *J. Phys. Chem. C*, 2011, **115**, 20618–20627.
60 C. S. Dong, M. L. Zhong, T. Huang, M. X. Ma, D. Wortmann, M. Brajdic and I. Kelbassa, *ACS Appl. Mater. Interfaces*, 2011, **3**, 4332–4338.
61 H. Z. Bao, W. H. Zhang, D. L. Shang, Q. Hua, Y. S. Ma, Z. Q. Jiang, J. L. Yang and W. X. Huang, *J. Phys. Chem. C*, 2010, **114**, 6676–6680.
62 Y. J. Xiong, Z. Q. Li, R. Zhang, Y. Xie, J. Yang and C. Z. Wu, *J. Phys. Chem. B*, 2003, **107**, 3697–3702.
63 M. L. Pang and H. C. Zeng, *Langmuir*, 2010, **26**, 5963–5970.
64 J. X. Fang, S. Lebedkin, S. C. Yang and H. Hahn, *Chem. Commun.*, 2011, **47**, 5157–5159.
65 P. Lignier, R. Bellabarba and R. P. Tooze, *Chem. Soc. Rev.*, 2012, **41**, 1708–1720.
66 G. R. Zhang, D. Zhao, Y. Y. Feng, B. S. Zhang, D. S. Su, G. Liu and B. Q. Xu, *ACS Nano*, 2012, **6**, 2226–2236.
67 S. D. Sun, X. P. Song, Y. X. Sun, D. C. Deng and Z. M. Yang, *Catal. Sci. Technol.*, 2012, **2**, 925–930.
68 Y. H. Liang, L. Shang, T. Bian, C. Zhou, D. H. Zhang, H. J. Yu, H. T. Xu, Z. Shi, T. R. Zhang, L. Z. Wu and C. H. Tung, *CrystEngComm*, 2012, **14**, 4431–4436.
69 K. E. DeKrafft, C. Wang and W. B. Lin, *Adv. Mater.*, 2012, **24**, 2014.
70 F. Hong, S. D. Sun, H. J. You, S. C. Yang, J. X. Fang, S. W. Guo, Z. M. Yang, B. J. Ding and X. P. Song, *Cryst. Growth Des.*, 2011, **11**, 3694–3697.
71 M. Murdoch, G. I. N. Waterhouse, M. A. Nadeem, J. B. Metson, M. A. Keane, R. F. Howe, J. Llorca and H. Idriss, *Nat. Chem.*, 2011, **3**, 489–492.
72 W. Q. Cai, J. G. Yu, S. H. Gu and M. Jaroniec, *Cryst. Growth Des.*, 2010, **10**, 3977–3982.